Automated Activity Estimation of the Cold-Water Coral *Lophelia pertusa* by Multispectral Imaging and Computational Pixel Classification

HONGBO LIU,[a,b] JANINA V. BÜSCHER,[b] KEVIN KÖSER,[b] JENS GREINERT,[b,c] HONG SONG,[a] YING CHEN,[a,d] AND TIMM SCHOENING[b]

[a] *Ocean College, Zhejiang University, Zhoushan, China;* [b] *GEOMAR Helmholtz Centre for Ocean Research Kiel, Kiel, Germany;* [c] *Institute of Geosciences, Christian-Albrechts University Kiel, Kiel, Germany;* [d] *State Key Laboratory of Fluid Power and Mechatronic Systems, Zhejiang University, Hangzhou, China*

(Manuscript received 22 August 2019, in final form 29 June 2020)

ABSTRACT: The cold-water coral *Lophelia pertusa* builds up bioherms that sustain high biodiversity in the deep ocean worldwide. Photographic monitoring of the polyp activity represents a helpful tool to characterize the health status of the corals and to assess anthropogenic impacts on the microhabitat. Discriminating active polyps from skeletons of white *Lophelia pertusa* is usually time consuming and error prone due to their similarity in color in common red–green–blue (RGB) camera footage. Acquisition of finer-resolved spectral information might increase the contrast between the segments of polyps and skeletons, and therefore could support automated classification and accurate activity estimation of polyps. For recording the needed footage, underwater multispectral imaging systems can be used, but they are often expensive and bulky. Here we present results of a new, lightweight, compact, and low-cost deep-sea tunable LED-based underwater multispectral imaging system (TuLUMIS) with eight spectral channels. A branch of healthy white *Lophelia pertusa* was observed under controlled conditions in a laboratory tank. Spectral reflectance signatures were extracted from pixels of polyps and skeletons of the observed coral. Results showed that the polyps can be better distinguished from the skeleton by analysis of the eight-dimensional spectral reflectance signatures compared to three-channel RGB data. During a 72-h monitoring of the coral with a half-hour temporal resolution in the laboratory, the polyp activity was estimated based on the results of the multispectral pixel classification using a support vector machine (SVM) approach. The computational estimated polyp activity was consistent with that of the manual annotation, which yielded a correlation coefficient of 0.957.

KEYWORDS: Ocean; In situ oceanic observations; Classification; Spectral analysis/models/distribution; Support vector machines

1. Introduction

The cold-water coral *Lophelia pertusa* is a widespread reef-building scleractinian coral species (Roberts et al. 2006, 2009). It is azooxanthellate (lacking symbiotic dinoflagellates) and feeds on food particles that rain through the water column from surface water or are transported laterally (Roberts and Anderson 2002; Roberts et al. 2006, 2009).

Lophelia pertusa reef systems are considered as biodiversity hotspots in deep water (Fosså et al. 2002; Freiwald et al. 2004) as shown in Fig. 1a. They process organic matter and recycle inorganic matter at the seafloor (van Oevelen et al. 2009; Baussant et al. 2018), and their complex aragonite structures provide hard substrate for a variety of benthic fauna (Fosså et al. 2002; Brooke and Young 2009). For instance, the coral reef microhabitats support higher shrimp abundance than the surrounding coral rubble or nonbiogenic sediment microhabitats (Purser et al. 2013; Osterloff et al. 2016c). In addition, they are important paleoenvironmental archives owing to their longevity over geological time scales, cosmopolitan distributions, and banded skeletal structure (Roberts et al. 2006, 2009).

Today, *Lophelia pertusa* bioherms suffer from anthropogenic threats. Direct impacts of human activities include physical damage by bottom trawling, exposure to sediment resuspension (caused by trawls or anchors), and discharge of sediments and minerals from hydrocarbon drilling and seabed mining (Freiwald et al. 2004; Buhl-Mortensen et al. 2015). Ocean acidification caused by anthropogenic carbon dioxide emissions also affects scleractinian corals, whose calcification rate decreases with declining seawater pH and carbonate ion concentrations, which results in slower growth followed by potential coral death (Roberts et al. 2006, 2009; Albright et al. 2016; Büscher et al. 2017).

Polyp activity of *Lophelia pertusa* is a good indicator of the coral health and thus a robust indicator of the environmental stress acting on the coral (Roberts and Anderson 2002; Buhl-Mortensen et al. 2015). Generally, polyps of *Lophelia pertusa* have no clear diurnal pattern (Mortensen 2001; Roberts and Anderson 2002; Baussant et al. 2018). They behave asynchronously on the same colony, and have a great variability across reefs (Purser 2015). *Lophelia pertusa* preys through expansions and retractions of the polyps; therefore, current velocity clearly impacts food capture efficiency (Roberts and Anderson 2002; Orejas et al. 2016). Under increased particle exposure, polyps can clean their surface effectively using a combination of mucus production, ciliary movement, and tentacular activity (Larsson and Purser 2011; Erftemeijer et al. 2012; Larsson et al. 2013; Buhl-Mortensen et al. 2015;

Denotes content that is immediately available upon publication as open access.

Corresponding author: Hongbo Liu, hbliu104@zju.edu.cn

DOI: 10.1175/JTECH-D-19-0139.1

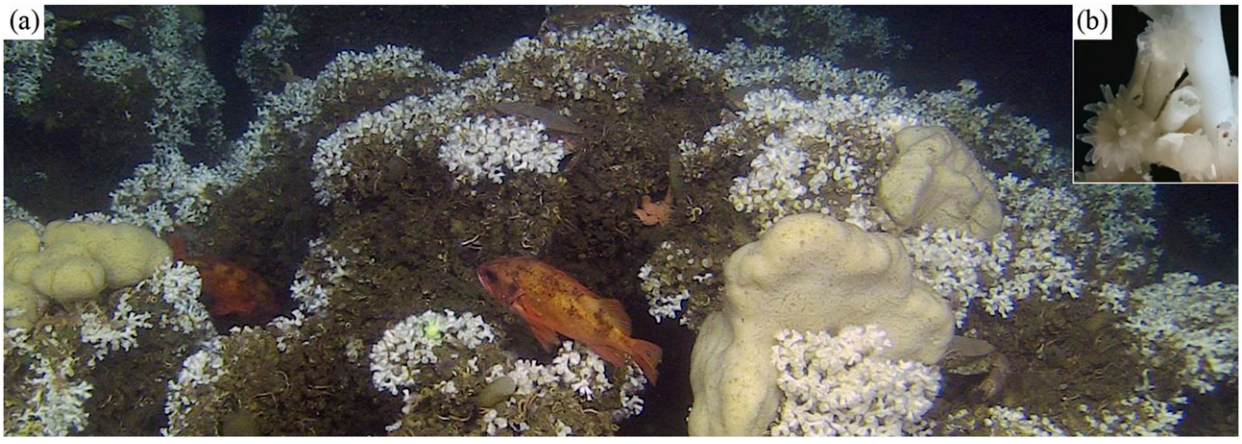

FIG. 1. The cold-water coral *Lophelia pertusa* reef sustain habitats for diverse fauna. (a) *Mycale lingua* sponges, *Sebastes viviparous* (redfish), and *Cancer pagurus* (edible crabs) are surrounded by white *Lophelia pertusa* colonies in this photo taken from the manned submersible JAGO diving at the Tisler Reef in Norway during the R/V *Poseidon* cruise POS526 (Greinert and Schoening 2019). (b) A close-up photograph of a branch of white *Lophelia pertusa* whose polyps and skeletons are similar in color.

Zetsche et al. 2016). Interactive effects of multiple climate change stressors comprising CO_2 concentration, temperature, and nutritional status on different physiological processes of *Lophelia pertusa* have been investigated in a multifactorial long-term experiment (Büscher et al. 2017). Monitoring of *Lophelia pertusa* helps distinguishing the natural behavior from stressed or disturbed behavior of the polyps (Larsson et al. 2013; Buhl-Mortensen et al. 2015), thus assessing the health status of the coral and the anthropogenic impacts on these important and nice microhabitats.

Photographic mapping is prevalent for quantitative assessment of the distribution and living condition of coral habitats. It benefits from high spatial resolution and exclusive color information compared to acoustic mapping. And it is noninvasive compared to assessments of the coral status (e.g., living biomass and respiration rates) through direct sampling (Purser 2015). Images are usually taken from a manned submersible (Greinert and Schoening 2019; Form et al. 2015) or from a remotely operated vehicle (ROV) (Purser et al. 2009, 2013; Purser 2015; Buhl-Mortensen et al. 2015), which is movable and thus flexible for mapping. Studies can also be done with a fixed camera system on the seafloor, which is capable of locally monitoring over a longer time enabling the detection of long-term variations (Barnes et al. 2013; Godø et al. 2014; Form et al. 2014). In this regard, cabled ocean observatories equipped with imaging devices are advantageous in continuously monitoring changes of visual features such as size, context, and color of coral structures (Osterloff et al. 2016a,b). The temporal scales range from days (Buhl-Mortensen et al. 2015) to months (Osterloff et al. 2016b, 2019), with an hourly or half-hourly temporal resolution. The spatial focus ranges from the level of colonies (Osterloff et al. 2016b) down to individual polyps (Osterloff et al. 2016a).

Analysis of the coral images by human experts is feasible but is often time consuming and error prone (Osterloff et al. 2016a,b; Schoening et al. 2016) in respect of accuracy and reproducibility. Typically, the polyp expansion state is manually annotated in different levels from fully expanded to retracted (Purser 2015; Buhl-Mortensen et al. 2015; Osterloff et al. 2016a), and the number of living or dead polyps is counted to calculate mortality (Brooke and Young 2009; Büscher et al. 2017). Apart from the limited visibility in water, visually distinguishing polyps is generally challenging. The semitransparent tentacles are fuzzy and often overlapping (Osterloff et al. 2016a). Expansion states of tentacles can be blurred by currents, and the size of polyps may be misinterpreted as the expansion state (Buhl-Mortensen et al. 2015). Moreover, human observers tend to overlook active polyps when many active ones occur in one image, therefore underestimate the activity (Osterloff et al. 2016a). An objective method is to take the silhouettes of a coral colony with and without extended polyps, respectively. The polyp activity is subsequently estimated from the difference of the pixel area between the two silhouettes (Roberts and Anderson 2002; Orejas et al. 2016; Baussant et al. 2018). However, given the featureless interior of a silhouette, this method requests for coral colonies selected and disposed with clearly observable polyps extending outwards against a dark background. Recently, machine learning aided image processing and analysis has been effectively used in recognition and classification of living corals (Purser et al. 2009; Osterloff et al. 2016a; Rimavicius and Gelzinis 2017; Nilssen et al. 2017). Osterloff et al. (2019) successfully linked the polyp activity determined by machine learning to other sensor time series (current, water depth, temperature) to find relationships. The potential of deep learning methods to utilize the enormous number of images taken by conventional red–green–blue (RGB) cameras has also been investigated (King et al. 2018).

Underwater hyperspectral imaging (UHI) and multispectral (MS) imaging methods benefit from both spatial and spectral information, thus they are promising for efficient seafloor habitat classification (Johnsen et al. 2013; Tegdan et al. 2015; Johnsen et al. 2016; Bongiorno et al. 2018), inorganic material classification at wreck sites for marine archaeology (Ødegård et al. 2018), and benthic mapping of sulfide mineral deposits (Sture et al. 2017) and manganese nodules (Dumke et al. 2018a).

UHI and MS imaging have also been effectively used in taxonomic studies of biological species such as spoon worms, sponges (Pettersen et al. 2014), coralline algae (Mogstad and Johnsen 2017) and megafauna (Dumke et al. 2018b), where different pigment compositions feature varying spectral absorption and reflection. However, underwater spectral imaging equipment have not been widely used because they are often expensive and bulky.

As to *Lophelia pertusa*, metabolic carotenoids bounding to specific proteins and to calcium carbonate contribute to spectral absorbance signatures of different coral segments (i.e., polyps and skeletons), where carotenoid proteins are only present in living polyps (Elde et al. 2012). Therefore, underwater hyperspectral imaging is used in the laboratory to determine polyp mortality and health conditions varying from unaffected to dead when exposed to a toxic compound (Letnes et al. 2019). Moreover, a periodic color change of *Lophelia pertusa* (i.e., living corals become more reddish from April to August, and recover until November) has been observed during a long-term in situ monitoring by using an RGB camera over 7 months (Osterloff et al. 2016b, 2019).

In this study, we took advantage of the recently introduced tunable LED-based underwater multispectral imaging system (TuLUMIS) (Liu et al. 2018) to provide an approach for automated estimation of polyp activity. TuLUMIS synchronizes a monochrome camera with flashing, pressure neutral color LEDs to provide eight-channel spectral images (while RGB cameras provide images with only three channels, i.e., red, green, and blue). It features a durable and simpler structure to reduce the bulk and cost compared to existing underwater multispectral imaging equipment. Different segments of *Lophelia pertusa* (i.e., polyps and skeletons) appear similar in color in common RGB camera footage as shown in Fig. 1b. Finer-resolved spectral reflectance at each pixel contains more information of the spectral signature, which might increase the contrast between coral polyps and skeletons and hence it might help an automated recognition of the polyps. We quantitatively compared the eight-channel MS imaging with RGB imaging on the ability of pixel-level classification of polyps versus skeletons using a similarity assessment criterion and a supervised classification [support vector machines (SVMs)]. The polyp activity estimation based on the computational pixel classification was validated through a 72-h monitoring of *Lophelia pertusa* in the laboratory.

The main contribution of this study lies in the effective application of TuLUMIS in polyp recognition and activity monitoring of the cold-water coral *Lophelia pertusa* in the laboratory condition. It supports and facilitates the attempt of using a multispectral imaging system such as TuLUMIS for an in situ activity monitoring of *Lophelia pertusa* in the future.

This paper briefly describes the principles of underwater multispectral imaging, the spectral similarity assessment, the classifier for coral segments, and the polyp activity estimation algorithm in section 2. Composition and specification of TuLUMIS and the experimental settings are presented in section 3, followed by the presentation of results in section 4. Spectral characteristics of *Lophelia pertusa* acquired during the monitoring are analyzed in section 5 followed by a discussion of potential improvements to make the most of the MS data and an attempt of a simplified annotation alternative. Finally, conclusions are drawn in section 6.

2. Principles and methods

a. Acquisition of spectral signatures

In underwater MS imaging, a significant portion of multispectral light is absorbed by water in dependence of the wavelength. Light attenuation is also affected by variable composition and concentration of constituents (e.g., pigments in phytoplankton, suspended particles, colored dissolved organic matter, and bubbles) in natural waters (Mobley et al. 2018).

To acquire the inherent spectral reflectance at the surface of the target for further analysis, it is necessary to eliminate the effects of inhomogeneous spectral illumination and attenuation in water. A white board featuring equal spectral reflectance through all visible light bands is usually used as a reference to correct the spectral distortion. As a result, each spatial pixel x relates to a spectral vector $\mathbf{x} = [x_1, x_2, \ldots, x_n]^{\mathrm{T}}$ with n relative reflectance calibrated by the white board from different channels. The spectral vector $\mathbf{x} \in \mathbb{R}^n$ describes the spectral signature of that pixel.

b. Spectral angle mapping and similarity assessment

For a specific spectral imagery acquisition method, the similarity between spectral signatures can be effectively measured by a spectral angle mapper (SAM) calculation (Zawada and Mazel 2014). SAM describes the angle θ between two spectral vectors in an n-dimensional space as

$$\Gamma(\mathbf{x}, \mathbf{y}) = \theta = \arccos \frac{\mathbf{x} \cdot \mathbf{y}}{\|\mathbf{x}\| \|\mathbf{y}\|}, \quad \mathbf{x}, \mathbf{y} \in \mathbb{R}^n, \tag{1}$$

where $\mathbf{x} = [x_1, x_2, \ldots, x_n]^{\mathrm{T}}$ and $\mathbf{y} = [y_1, y_2, \ldots, y_n]^{\mathrm{T}}$ are spectral signatures ($\mathbb{R}^{n \times 1}$ vectors) extracted from the two pixels x and y. A smaller $\Gamma(\mathbf{x}, \mathbf{y})$ indicates a higher similarity between $\mathbf{x}$ and $\mathbf{y}$, and it attains a value of 0 for equal spectral signatures.

In this study, two spectral imagery acquisition methods (i.e., with TuLUMIS and an RGB camera) were used to collect spectral vectors of two different classes of objects (i.e., polyps and skeletons of *Lophelia pertusa*). The spectral vectors collected with TuLUMIS were represented by $\mathbf{p}^{\mathrm{MS}}$ and $\mathbf{s}^{\mathrm{MS}} \in \mathbb{R}^8$ for polyp and skeleton pixels, respectively. The spectral vectors collected with an RGB camera were represented by $\mathbf{p}^{\mathrm{RGB}}$ and $\mathbf{s}^{\mathrm{RGB}} \in \mathbb{R}^3$ for polyp and skeleton pixels, respectively. Apart from different dimensionalities, the acquisitions of deterministic spectrum of an object by different methods are often subject to spectral variabilities (i.e., inhomogeneous surface composition, media condition and sensor noise, etc.) in practice (Manolakis et al. 2003). As a result, SAM measures across acquisition methods such as $\Gamma(\mathbf{p}^{\mathrm{MS}}, \mathbf{s}^{\mathrm{MS}})$ and $\Gamma(\mathbf{p}^{\mathrm{RGB}}, \mathbf{s}^{\mathrm{RGB}})$ were not directly comparable. Besides, within-class deviations were brought in spectral signatures of different pixels of the same object.

To compare the ability of polyp–skeleton discrimination between different imaging modalities, a normalized dissimilarity assessment criterion derived from SAM measures was

used. Suppose there were m_p pixels of polyps and m_s pixels of skeletons collected by each method, and the mark of methods (RGB or MS) was omitted in the following derivation for the sake of brevity. For a certain imaging modality, spectral signatures extracted from polyp and skeleton pixels were represented as $\mathbf{p}_i (i = 1, \ldots, m_p)$ and $\mathbf{s}_i (i = 1, \ldots, m_s)$. The within-class similarities of the m_p polyp pixels and the m_s skeleton pixels were estimated as

$$\mu^{(\Gamma)} = \frac{\sum_{i=1}^{m_p}\sum_{j=1}^{m_p}\Gamma(\mathbf{p}_i, \mathbf{p}_j) + \sum_{i=1}^{m_s}\sum_{j=1}^{m_s}\Gamma(\mathbf{s}_i, \mathbf{s}_j)}{m_p(m_p - 1) + m_s(m_s - 1)} \tag{2}$$

and the spectral similarity measured by SAM between each pair of polyp and skeleton pixels was modified as

$$\Delta_{ij}^{(\Gamma)} = \Gamma(\mathbf{p}_i, \mathbf{s}_j) - \mu^{(\Gamma)}, \tag{3}$$

where $\Delta_{ij}^{(\Gamma)}$ represents the modified between-class similarity of $\mathbf{p}_i$ and $\mathbf{s}_j$ with $i = 1, 2, \ldots, m_p$ and $j = 1, 2, \ldots, m_s$. The normalized spectral similarity between the polyp class and the skeleton class was then calculated by

$$\delta^{(\Gamma)} = \frac{\sum_{i=1}^{m_p}\sum_{j=1}^{m_s}\Delta_{ij}^{(\Gamma)}}{m_p \times m_s}, \tag{4}$$

which is the average of the modified between-class spectral similarities across the selected m_p polyp pixels and the m_s skeleton pixels. A larger $\delta^{(\Gamma)}$ indicates a larger divergence estimated by the corresponding imaging modality. It allows a quantitative comparison of the MS method using TuLUMIS to the conventional RGB method for their ability to discriminate the polyp pixels from the skeleton pixels by comparing $\delta^{(\mathrm{MS},\Gamma)}$ and $\delta^{(\mathrm{RGB},\Gamma)}$.

c. SVM classifier and metrics

Compared to the RGB method which has only three spectral channels, the MS method provides eight spectral channels over the same visible spectrum from 400 to 700 nm. To evaluate the benefits of the finer-resolved spectral information to the classification of polyps and skeletons, SVM (Schölkopf et al. 1997) classifiers were trained and deployed on individual pixelwise spectral features without including shape and texture information.

The performance of each classifier was evaluated by a confusion matrix of which the columns and rows represent the instances in a predicted class and an actual class, respectively. Manually annotated labels (i.e., polyp, skeleton, or background) were treated as actual classes to check if the SVM classifier predicted correctly.

For a binary (positive–negative) classification, its 2 × 2 confusion matrix consists of the number of true positive (TP) for correctly classified positive cases, false positive (FP) for incorrectly classified positive cases, true negative (TN) for correctly classified negative cases, and false negative (FN) for incorrectly classified negative cases. Sensitivity and specificity are common metrics of the classification accuracy, which are defined as the correctly classified proportion of the positive and negative cases, respectively, as follows:

$$\text{Sensitivity} = \frac{\text{TP}}{\text{TP} + \text{FN}}, \tag{5}$$

$$\text{Specificity} = \frac{\text{TN}}{\text{TN} + \text{FP}}. \tag{6}$$

For a skewed dataset with a disparity in the number of instances between classes, a geometric mean (G-mean) of the sensitivity and the specificity is used to evaluate the classification accuracy on both the positive and negative classes in a balanced way (Akosa 2017):

$$\begin{aligned}\text{G-mean}_2 &= \sqrt{\text{Sensitivity} \times \text{Specificity}} \\ &= \sqrt{\frac{\text{TP}}{\text{TP} + \text{FN}} \times \frac{\text{TN}}{\text{TN} + \text{FP}}}.\end{aligned} \tag{7}$$

For our ternary classification of polyps, skeletons, and the background, a 3 × 3 matrix was constructed where the number of correctly classified instances lay on the main diagonal. The three-class G-mean was calculated by the geometric mean of sensitivities of the three classes:

$$\text{G-mean}_3 = \sqrt[3]{\frac{\text{TP}_p}{\text{TP}_p + \text{FN}_p} \times \frac{\text{TP}_s}{\text{TP}_s + \text{FN}_s} \times \frac{\text{TP}_b}{\text{TP}_b + \text{FN}_b}}, \tag{8}$$

where $\text{TP}_{p,s,b}$ and $\text{FN}_{p,s,b}$ are referred to the three binary tests, namely, polyp–nonpolyp, skeleton–nonskeleton, and background–nonbackground. Individual G-mean$_2$ for each of the three binary tests was also calculated to evaluate the classification of a specific class.

d. Polyp activity estimation

Polyp activity was estimated by the proportion η_p of pixels classified as polyp in each of the m images:

$$\eta_p^i = \frac{N_p^i}{w \times h}, \quad i = 1, 12, \ldots, m, \tag{9}$$

where N_p^i represents the number of pixels classified as polyp in image i; w and h denote the width and height of the image in pixels. To emphasize the temporal dynamics, a sequence of estimated activities $[\eta_p^1, \eta_p^2, \ldots, \eta_p^m]$ were standardized by subtracting their mean and divided by their standard deviation:

$$\hat{\eta}_p^i = \frac{\eta_p^i - \overline{\eta}_p}{\sigma(\eta_p)}, \quad i = 1, 2, \ldots, m, \tag{10}$$

where

$$\overline{\eta}_p = \frac{1}{m}\sum_{i=1}^{m}\eta_p^i, \tag{11}$$

$$\sigma(\eta_p) = \sqrt{\frac{1}{m}\sum_{i=1}^{m}(\eta_p^i - \overline{\eta}_p)^2}. \tag{12}$$

3. Experiment

a. *Specimen of* Lophelia pertusa

A healthy branch of white *Lophelia pertusa* with 20 polyps shown in Fig. 2 was selected from specimens cultivated in a climate room as the object of the monitoring.

The laboratory cultured colonies were carefully collected during a cruise in August 2014 from the Nord-Leksa reef in the outer Trondheim Fjord (location approx. 63°36.5′N, 09°22.9′E).

b. *Experimental setup*

For the MS method, TuLUMIS was used in the coral monitoring experiment as shown in Fig. 3a. Spectral images were collected by a 12-bit industrial monochrome camera (acA2040–25gmNIR, Basler, Germany) with an Apo-Xenoplan 2.0/24 lens (Schneider, Germany) illuminated by eight pairs of custom color LEDs (LUXEON Z, Lumileds, Netherlands). A minicomputer (NUC6i5SYB, Intel, United States) and a microcontroller (Arduino MKR Zero, Italy) synchronized the lighting and image acquisition. A set of watertight cables (SubConn Micro Circular, MacArtney, Denmark) were used for power and signal transmission.

The layout of the experiment is shown in Fig. 3b. A lampshade as shown in Fig. 3c was used to hold the LEDs and the camera. The eight pairs of LEDs were evenly distributed in a circle on the conical wall of the lampshade. The oppositely fixed LED pairs provided a homogeneous illumination of the coral to alleviate shadows. The monochrome camera was mounted in the middle of the lampshade. The lampshade was hung approximately 30 cm above the coral sample and was submerged in the water tank.

The computer synchronized the exposure of the camera and the flash of a pair of LEDs to take an image at a specific spectral band. A white board was used as a reference to balance the LED power for each band by tuning the pulse width of their driving voltage, as well as to adjust the exposure time of the camera, in order to compensate the spectral distortion between images of different wave bands.

For comparison, a common RGB imaging system was used to image the same coral sample at the same condition. Given its generality and feasibility, the camera of a cellphone (F5121, Sony, Japan) was used as the RGB sensor, and the coral was illuminated by a 700 lm white LED torch (XM-L2, CREE, United States).

c. *Monitoring settings*

The monitoring was conducted in a totally dark climate room where the corals were cultured. The selected *Lophelia pertusa* branch fixed on a substrate was settled in a 40 cm × 40 cm × 40 cm water tank filled with natural seawater from the North Sea circulated by a streaming pump with the flow rate of 900 L h^{-1} (Koralia Nano, Hydor, Italy). The coral was fed 24 h before the monitoring with freshly hatched *Artemia franciscana* nauplii (Premium, Sanders) and calanoid copepods (Goldpods liquid zooplankton concentrate, Nyos, Germany). The temperature and salinity were kept constant at 7.5°C and 35 psu, respectively.

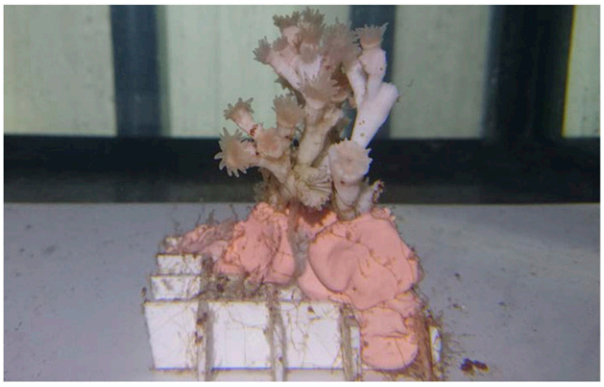

FIG. 2. The white *Lophelia pertusa* branch used in the experiment.

The monitoring lasted for 72 h. An automated imaging procedure was programmed to carry out an acquisition every half hour. For each acquisition, eight images at different wave bands were taken sequentially within one second before the polyps moved significantly. As a prerequisite, the flash of LEDs in complete darkness is not a significant stimulator of polyp expansion or behavior (Mortensen 2001).

4. Results

a. *Description of datasets*

To evaluate the spectral discrimination ability of the MS method with respect to the RGB method, an eight-channel spectral image and a three-channel RGB image of the same branch of *Lophelia pertusa* were selected to make up a comparative group.

As shown in Fig. 4, the two images were cropped to the same size of 1200 × 1200 pixels. The MS image shown here is a synthetic fusion of the set of gray-value multispectral images for the purpose of visualization, while reflectance spectra of the MS image is analyzed in section 5a in detail. As to the fusion process, spectral response curves of the RGB image sensor provided by the manufacturer were used to convert an eight-channel spectral image to a color image. At each pixel, eight intensities weighted by the spectral response at their corresponding central wavelength were added together, and the aggregated RGB intensities were normalized by dividing a white point which has the largest intensity over the RGB channels in the image.

The RGB image and the MS-fused image were manually annotated in three classes: polyps, skeletons, and the background. As shown in Fig. 4, the author Hongbo Liu drew three masks in the GNU Image Manipulation Program (GIMP) with a graphic tablet (CTL-490DW-S, Wacom, United States) to set up a gold standard of the pixelwise three-class annotation after the acquisition. A year later, the same person annotated the two images again to check the consistency of the gold standard. Since the images were collected in close proximity to a single branch of *Lophelia pertusa* in the laboratory condition with sufficient illumination, the intraobserver agreement reached over 99% with differences only appeared at the edges of the polyps.

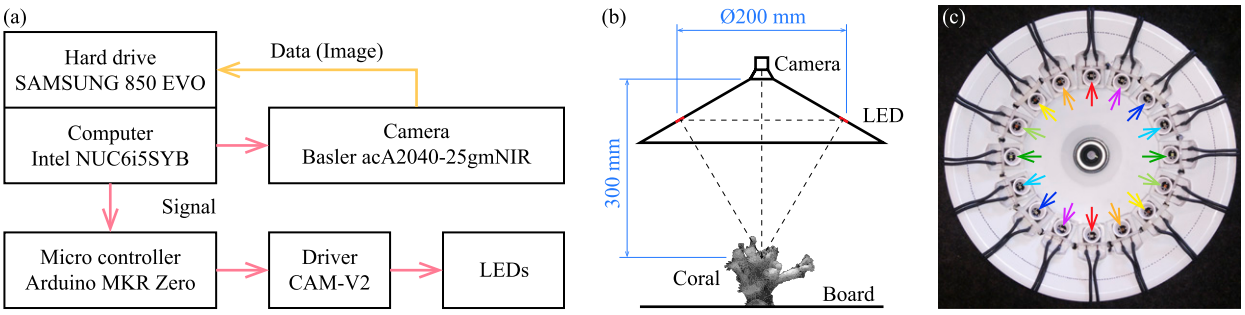

FIG. 3. Setup of TuLUMIS for the monitoring experiment. (a) Scheme of TuLUMIS where a computer synchronized a camera and a series of LEDs for imaging. (b) Layout of the monitoring experiment. Eight pairs of LEDs were evenly distributed in a circle on a lampshade, and the camera was mounted in the middle. The lampshade was submerged right above the coral sample in the water tank. (c) Front view of the lampshade. Each pair of LEDs were fixed oppositely, and their colors are indicated by the arrows.

The annotated RGB image and MS-fused image in the comparative group made up two datasets RGB_{cmp} and MS_{cmp} containing 1 440 000 instance-label pairs corresponding to one full image with three and eight features, respectively. To train and test SVM classifiers, The datasets RGB_{cmp} and MS_{cmp} were further divided into training–validation datasets ($RGB_{t\text{-}v}$, $MS_{t\text{-}v}$) and test datasets (RGB_{test}, MS_{test}). The training–validation datasets $RGB_{t\text{-}v}$ and $MS_{t\text{-}v}$ were established by randomly selecting 28 800 pixels (accounting for 2% of the entire 1200 × 1200 pixels) from datasets RGB_{cmp} and MS_{cmp} with the proportion of the three classes remained. As a result, dataset $RGB_{t\text{-}v}$ consisted of 1252 (4.3%) pixels of polyps, 3554 (12.3%) pixels of skeletons, and 23 994 (83.3%) pixels of the background; dataset $MS_{t\text{-}v}$ consisted of 2388 (8.3%) pixels of polyps, 3763 (13.1%) pixels of skeletons, and 22 649 (78.6%) pixels of the background. The rest 98% instance-label pairs in datasets RGB_{cmp} and MS_{cmp} made up the test datasets RGB_{test} and MS_{test}, respectively.

During the 72-h monitoring with an acquisition period of 0.5 h, 144 eight-channel spectral images were acquired. To validate the activity estimation of the coral, 36 spectral images were selected from the monitoring sequence with an equal interval of 2 h to make up a verification group MS_{act}. For the 36 images in MS_{act}, only polyp pixels were annotated to derive a gold standard of the activity of the observed branch of *Lophelia pertusa*.

b. Spectral angle mapping and similarity assessment

To generally assess the improved capability of MS imaging over RGB in distinguishing polyp pixels from skeleton pixels, the criterion described in Eq. (4) was used. From the perspective of computational intensity, a random selection of 1000 pixels of polyps and 1000 pixels of skeletons from each dataset of RGB_{cmp} and MS_{cmp} were used to calculate $\Delta^{(RGB,\Gamma)}$ and $\Delta^{(MS,\Gamma)}$ with $m_p = m_s = 1000$. From the perspective of generality, the random selection was repeated for 10 000 times to cover the RGB_{cmp} and MS_{cmp} in order to check the stability of the results of the similarity assessment of $\delta^{(RGB,\Gamma)}$ and $\delta^{(MS,\Gamma)}$.

Histograms of $\delta^{(MS,\Gamma)}$ and $\delta^{(RGB,\Gamma)}$ of the 10 000 random selections were plotted together in Fig. 5. The distributions of $\delta^{(MS,\Gamma)}$ and $\delta^{(RGB,\Gamma)}$ are approximately normal with means of 1.78 and 1.15, and standard deviations of 0.124 and 0.102, respectively. Statistically, $\delta^{(MS,\Gamma)}$ lies in the range of 1.78 ± 0.24 (or between 1.54 and 2.02) while $\delta^{(RGB,\Gamma)}$ lies in the range of 1.15 ± 0.20 (or between 0.95 and 1.35) with a 95% of confidence. There is no intersection between these two 95% confidence intervals. Thus, a significant advantage of the MS modality over RGB on discrimination of polyps and skeletons can be inferred.

c. SVM classification

As the spectra of polyp and skeleton pixels overlapped each other and shown an unsharp divergence (which is clearly shown

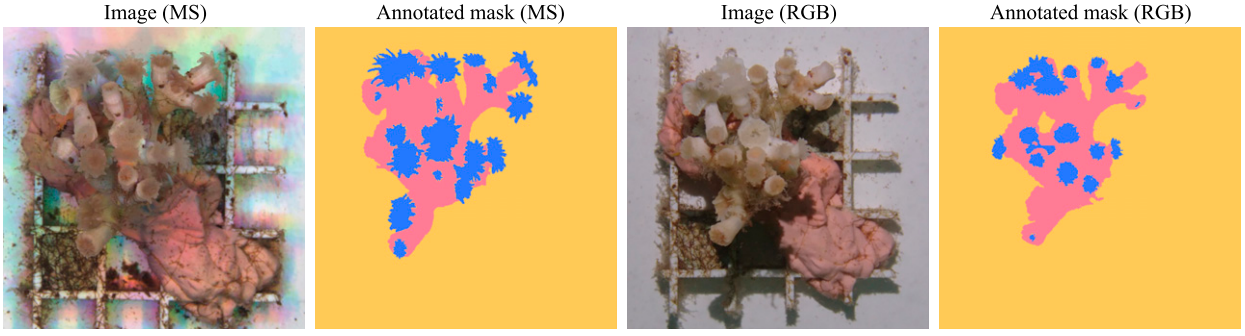

FIG. 4. Images acquired by the MS method and the RGB method for comparison and their annotation. The eight-channel spectral image acquired by the MS method was fused into RGB channels for visualization. The manually annotated classes (i.e., blue for polyp, pink for skeleton, and yellow for background) were derived to be a gold standard in the following analysis.

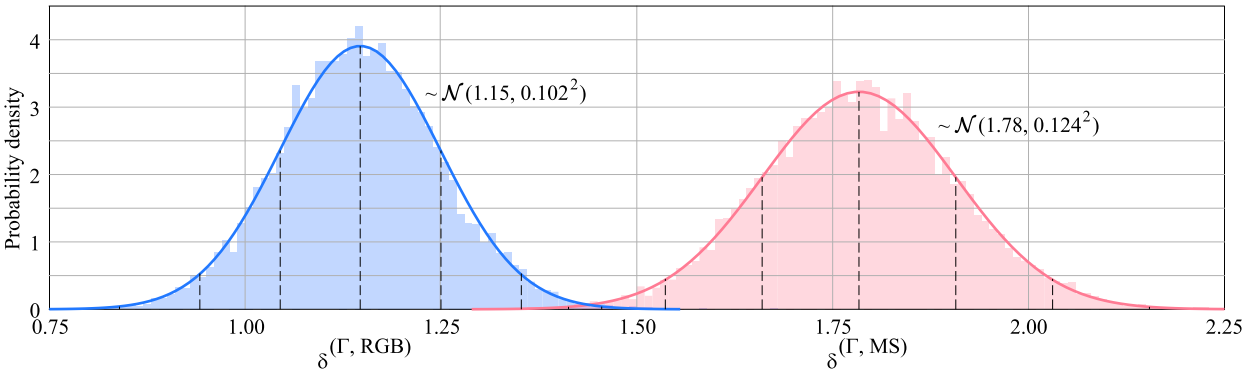

FIG. 5. Distributions of sample normalized spectral similarity $\delta^{(\mathrm{RGB},\Gamma)}$ and $\delta^{(\mathrm{MS},\Gamma)}$ between the polyp class and the skeleton class for the 10 000 randomly selected samples of size 1000. The two distributions are approximately normal. By statistical inference, $\delta^{(\mathrm{MS},\Gamma)}$ is larger than $\delta^{(\mathrm{RGB},\Gamma)}$ in terms of 95% confidence intervals which implies that it is easier for the MS method to discriminate polyps from skeletons thanks to its finer-resolved spectrum than the RGB method.

in Fig. 11d, and is discussed in section 5a), machine learning methods were used to compare between the MS and RGB modalities on their ability to classify pixels of polyps and skeletons. The comparison were based on individual pixelwise spectral features without shape and texture information. The machine learning toolbox scikit-learn (version 0.20.0) (Pedregosa et al. 2011) was used for data analysis and visualization. A brief test based on a subset of $\mathrm{MS}_{\text{t-v}}$ was conducted involving common machine learning algorithms including k-nearest neighbors, naive Bayes, logistic regression, and SVMs with linear and nonlinear kernels. The SVM with a nonlinear kernel turned out to have the best accuracy thus was chosen in the following analysis.

SVM classifiers with a radial basis function (RBF) kernel were trained with a fivefold cross validation over training-validation datasets $\mathrm{RGB}_{\text{t-v}}$ and $\mathrm{MS}_{\text{t-v}}$. A two-step grid search was conducted to find the best hyperparameters C and γ, where C is the penalty parameter and γ is the RBF kernel parameter (Hsu et al. 2003). The target of the grid search was to maximize the metric of the three-class G-mean_3 defined as Eq. (8). The first step used a parameter search grid increasing with the base of 10 and ranging from 10^{-4} to 10^{7}. The second step used a finer grid increasing with the base of 2, centered at the maximum of the first grid. The G-mean_3 of the second grid search step over $\mathrm{RGB}_{\text{t-v}}$ and $\mathrm{MS}_{\text{t-v}}$ are shown in Fig. 6. It can be seen that the G-mean_3 for the classifications of MS pixels are larger than that of the RGB pixels, and it indicates a better classification accuracy of the MS modality over RGB. For the MS grid search, a combination of $C = 4$ and $\gamma = 128$ resulted in the largest $\text{G-mean}_3 = 0.81$. For the RGB grid search, a combination of $C = 512$ and $\gamma = 512$ resulted in the largest $\text{G-mean}_3 = 0.69$.

After cross validation, the selected hyperparameters C and γ were used to train SVM classifiers on the entire $\mathrm{RGB}_{\text{t-v}}$ and $\mathrm{MS}_{\text{t-v}}$, respectively. The trained classifiers were tested on the corresponding training sets first. For the MS classifier deployed on $\mathrm{MS}_{\text{t-v}}$, the resulting G-mean_3 was 0.91, and the G-mean_2 of the three binary tests were 0.96, 0.90, and 0.96. Analogously, the RGB classifier deployed on $\mathrm{RGB}_{\text{t-v}}$ resulted a G-mean_3 of 0.68, and the G-mean_2 of the three binary tests were 0.69, 0.80, and 0.87.

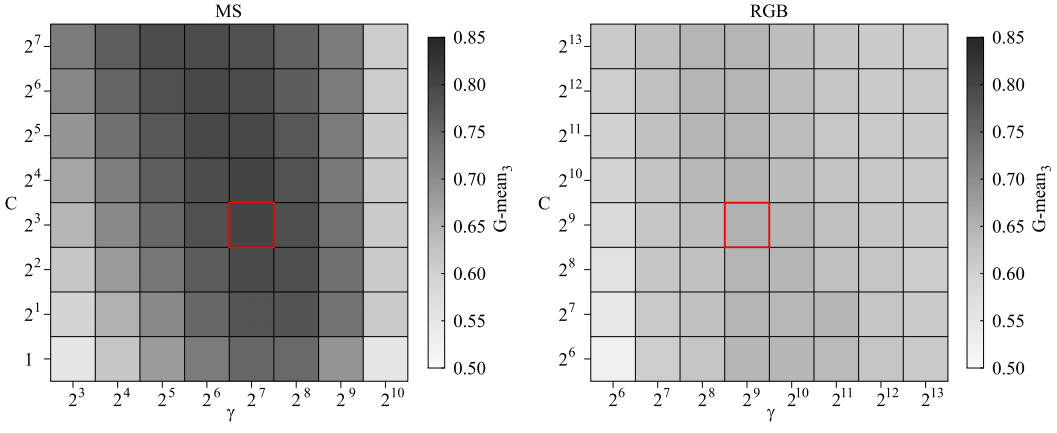

FIG. 6. Selection of the hyperparameters of C and γ in the SVM classifiers by grid searching. The G-mean_3 metric was used to evaluate the accuracy of the classification. The red boxes mark the combination of parameters resulted in the best accuracy. The darker shading in the MS grid illustrates a better classification accuracy by the MS imaging modality compared to RGB.

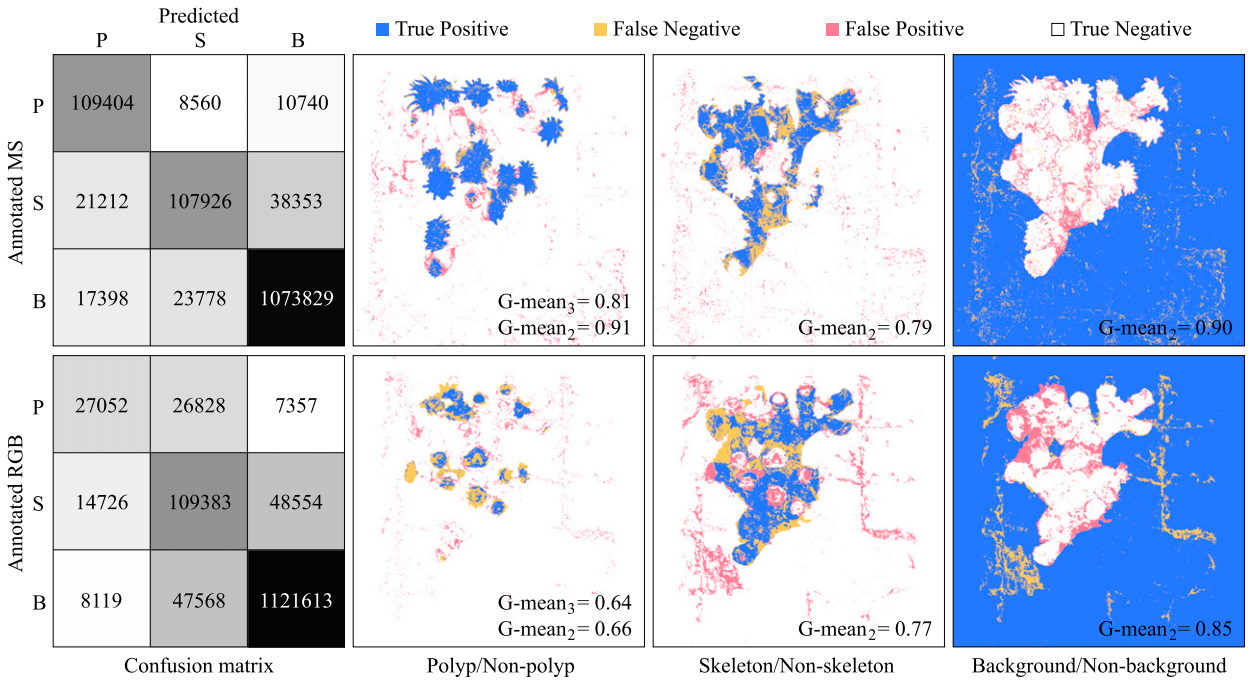

FIG. 7. Confusion matrices and visualized results of the three binary tests of the classifications of the MS and RGB images. The first column shows the confusion matrices of the classifications (*P* for polyp, *S* for skeleton, and *B* for background) of the MS and RGB test datasets, respectively, where a darker shading represents a larger number. The rest of the columns show the results of the binary test of polyp–nonpolyp, skeleton–nonskeleton, and background–nonbackground for the two images, respectively. Compared to the RGB classifier, the MS classifier features a similar ability to discriminate between the background and coral segments, but an improved ability to discriminate polyps from skeletons.

The trained classifiers were then tested on the test datasets RGB_{test} and MS_{test}. To quantitatively assess the classifiers, confusion matrices indicating the correctly and incorrectly classified pixels are shown in Fig. 7 along with the visualized results of the three binary tests, namely, polyp–nonpolyp, skeleton–nonskeleton, and background–nonbackground. For MS_{test}, the G-mean$_3$ was 0.81, and the G-mean$_2$ of the three tests were 0.91, 0.79, and 0.90. It seemed easier for the MS classifier to distinguish between background and nonbackground pixels than to distinguish between polyp and skeleton pixels. For RGB_{test}, the G-mean$_3$ was 0.64, and the G-mean$_2$ of the three tests were 0.66, 0.77, and 0.85. Those G-mean$_2$ demonstrate that the MS classifier has an improved ability to discriminate polyps from skeletons over the RGB classifier, while the two classifiers has a similar ability to discriminate coral segments (i.e., polyps and skeletons) from the background.

The RGB classifier seems underfitted in the classifications of $RGB_{t\text{-}v}$ and RGB_{test}. The so-called high bias problem is considered to result from insufficient features (only three) extracted from the three-channel RGB image. On the contrary, the MS classifier seems overfitted in the classifications of $RGB_{t\text{-}v}$ and RGB_{test}. The so-called high variance problem is considered to result from an insufficient size of the training set. In addition, MS_{test} was essentially extracted from the same images as $MS_{t\text{-}v}$. To get rid of the potential influence of similar neighboring pixels, another annotated MS image was used to make up a new dataset MS_{new} to further test the MS classifier for its generalization ability. Analogously, the confusion matrix and the visualized results of the three binary tests are shown in Fig. 8. In this case, the G-mean$_3$ was 0.72, and the G-mean$_2$ of the three tests were 0.87, 0.69, and 0.86. Compared to the performance on the dataset MS_{test}, the MS classifier generally keeps the ability of discriminating polyps from skeletons, and it shows a decreased ability of discriminating skeletons from the background. We further analysis the performance of the MS classifier and discuss its potential improvements in section 5b.

Note the misclassified pixels that clustered surrounding the corals branch, especially in the last two columns in Fig. 7 and in Fig. 8. When refered to Fig. 4, most of those misclassified pixels were recognized as the red spots and brownish threads covering the supportive latticed structures and the white board background. And those spots and threads mainly perturbed the classification of the skeleton pixels against background pixels. We discuss the source and impact of those substance in section 5a.

d. Polyp activity estimation

The trained MS classifier was then used on the 36 images in MS_{act} to classify polyp and nonpolyp pixels. The computational classified results were evaluated by the annotated gold standard to establish polyp–nonpolyp binary confusion matrices visualized in Fig. 9. The G-mean$_2$ of the 36 images for the polyp–nonpolyp tests ranged from 0.81 to 0.87. Compared with the G-mean$_2$ = 0.91 for the classification of the MS_{test} dataset and the G-mean$_2$ = 0.87 for the classification

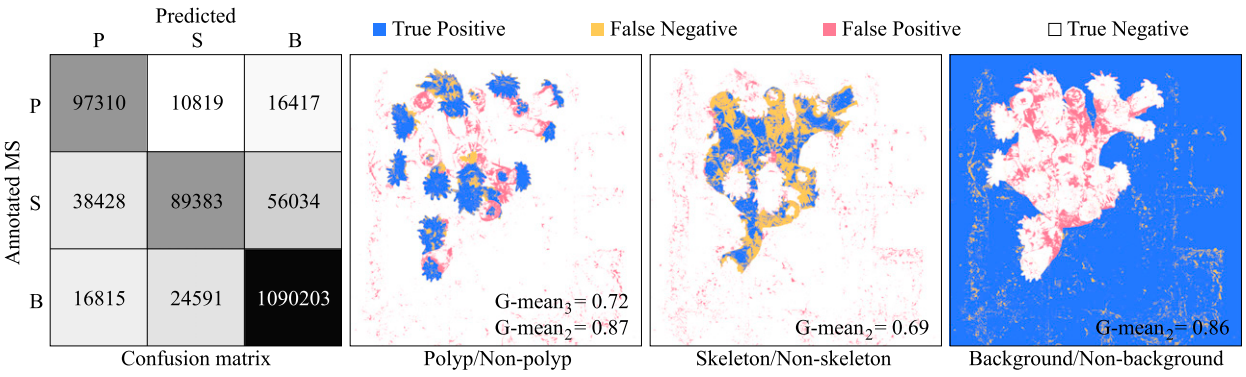

FIG. 8. Confusion matrix and visualized results of the three binary tests of the classifications of an independent MS image (i.e., dataset MS_{new}) to further test the generalization ability of the MS classifier. The subfigures share the same definition and style as those in Fig. 7. The MS classifier generally keeps the ability of discriminating polyps from skeletons and the background on the independent MS image.

of the independent MS image, the MS classifier featured a good generality.

Based on the classified polyp pixels in MS_{act}, the polyp activities were estimated using Eq. (10). The polyp activities derived from the annotated polyp pixels in MS_{act} were used to validate the estimated activities. In Fig. 10a, the estimated and annotated activities were plotted in a Cartesian coordinate system and illustrated a linear relationship. The linear relationship was fitted by the linear least squares method with the Pearson correlation coefficient of 0.957. By using Fisher's transformation (Fisher 1950), the 95% confidence interval of the Pearson correlation coefficient was calculated as between 0.917 and 0.978. It implies that the estimated activities are consistent with the annotated activities of the polyps. A root-mean-square deviation of the 36 scatter points was calculated to be 0.095. Based on the classified polyp pixels of all the 144 MS images (30 min between image captures), the polyp activity sequence of the entire 72-h monitoring was estimated and plotted in Fig. 10b.

5. Discussion

a. *Spectra of polyps and skeletons*

The averaged spectra of all the polyp and skeleton pixels in the MS image shown in Fig. 4 were plotted in the A0 panel of Fig. 11d. The spectrum of the averaged polyp pixels overlapped with the spectrum of the averaged skeleton pixels, while the former had a lower standard deviation. According to a study on pigments in white *Lophelia pertusa*, carotenoid proteins are only present in living polyps, which leads to an in vivo absorbance peak at 409 nm and an in vitro absorbance peak at 429 nm (Elde et al. 2012). However, the absorbance difference is not clear in the A0 panel of Fig. 11d. To elaborate on this, the whole A0 was divided into seven subareas A1 to A7 as marked out by boxes in Figs. 11a and 11b. The averaged spectra of all polyp and skeleton pixels in the subareas were plotted in Fig. 11d with the axes and legends defined in Fig. 11c.

By carefully looking at the coral in Fig. 4, the polyps had different transparency, and there were red spots and brownish threads distributed on the skeleton. The red spots were probably eggs of unhatched *Artemia* that aggregated on the skeleton. The brownish threads were hydrozoans that had been brought into the system during coral collection. Healthy corals are covered by a layer of coenosarc (or epithelium) which can be lost due to disturbance and might take some time to recover. The hydrozoans settle on the skeleton where the coenosarc is incomplete. Within the study on pigments in white *Lophelia pertusa* by Elde et al. (2012), polyps were pulled out using tweezers as in vivo samples and placed directly on seawater (filtered) soaked Whatman GF/C 25-mm glass fiber filters. And the in vitro sample was prepared by crushing frozen corals in a mortar followed by extracting and filtering to remain pigments without debris. While in our study, the semitransparent rough surface of polyps were directly imaged, and the skeletons were covered by different substances. We suggest that the varied skeleton spectra are due to the mottled skeletons with incomplete coenosarc and covered hydrozoans, while the varied polyp spectra are due to the rough surface of the semitransparent tentacles. As a result, the spectra of polyp and skeleton pixels in our in situ study were different from the results of Elde et al. (2012).

b. *Potential improvements*

Performance of different MS classifiers deployed on $MS_{t\text{-}v}$, MS_{test}, and MS_{new} is presented in Fig. 12. The MS classifiers were trained on different sizes of $MS_{t\text{-}v}$ range from 112 to 115 200. The relative time consumptions for training the corresponding classifiers were also plotted. As the size of the training set increases from 112 to 7200, the G-$mean_3$ and G-$mean_2$ of polyps for classifications of MS_{test} and MS_{new} grow progressively at a low time consumption. As the size of the training set continuous to increase, the G-$mean_3$ and G-$mean_2$ of polyps for classifications of MS_{test} and MS_{new} grow slowly but cost more and more time for training. The surge in time consumption is due to that the SVM with a nonlinear kernel is not efficient over large datasets. Therefore, other machine learning methods (such as neural network) can be used along with a "minibatch" or a "stochastic" training

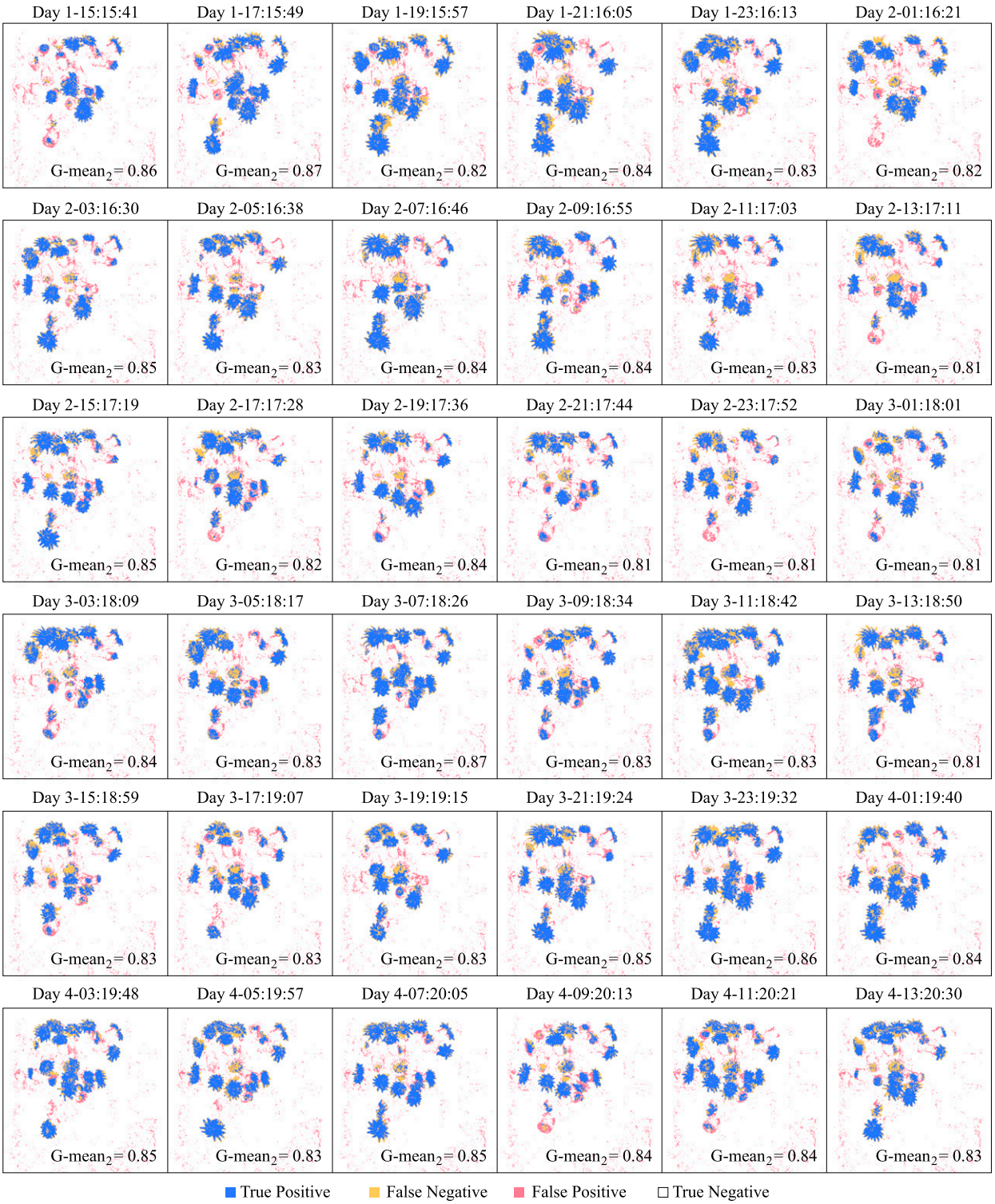

FIG. 9. Results of the binary tests of polyp–nonpolyp for the MS images in MS_{act} acquired throughout the 72-h monitoring with an interval of 2 h. The binary G-mean$_2$ of polyp–nonpolyp tests ranged between 0.81 and 0.87 for the 36 images.

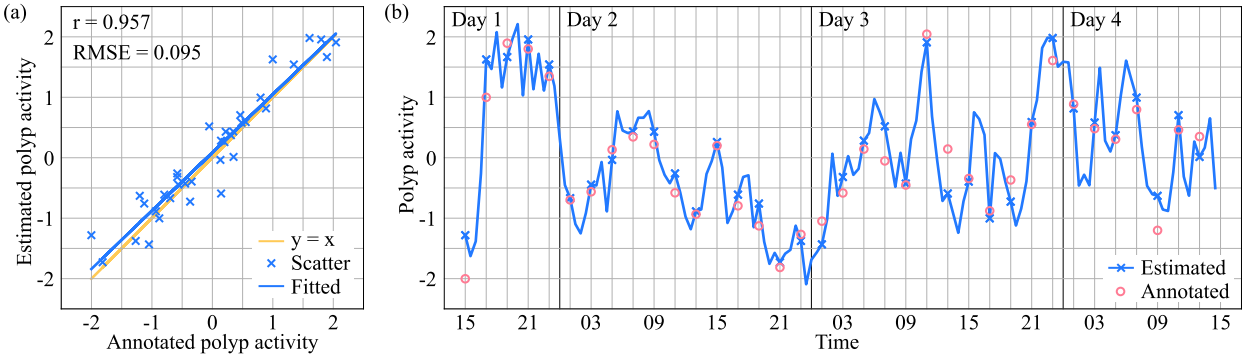

FIG. 10. Estimated and annotated activities of polyps. (a) A linear relationship between the estimated activities and the annotated activities for the 36 MS images in MS_{act}. Based on the classified polyp pixels of all the 144 MS images, (b) the estimated polyp activities during the entire 72-h monitoring with an interval of 0.5 h.

scheme to train a MS classifier with more data in order to solve the "high variance" problem.

In this study, the pixel-level classification based on single-pixel information did not take advantage of the neighbor pixel groups and context features, whereas these features can boost the classification accuracy once effectively used. A multispectral imaging system with a gray camera can provide (nonredundant) higher spectral resolution and higher spatial resolution (without Bayer pattern layer in an RGB camera). Thus, MS images can be potentially further optimized and might become better than the conventional RGB images for classifiers built with complex neural networks. Integrating other sensors such as a turbidity meter in the system can improve the interpretation of estimated activity. And for a long-term monitoring, the periodic change in each spectral channel becomes important.

c. *A simplified pixel annotation alternative*

Even the collected images in this study were clear and sharp enough for a person to discriminate polyps from skeletons, the mask based annotation was still time consuming. A simplified pixel annotation was conducted as a time-saving alternative. Pixels representing the three classes were manually picked from 12 MS images equally sampled (with an interval of 6 h) in the 72-h sequence. On each of these images, 200 sample pixels in total were selected randomly comprising representative

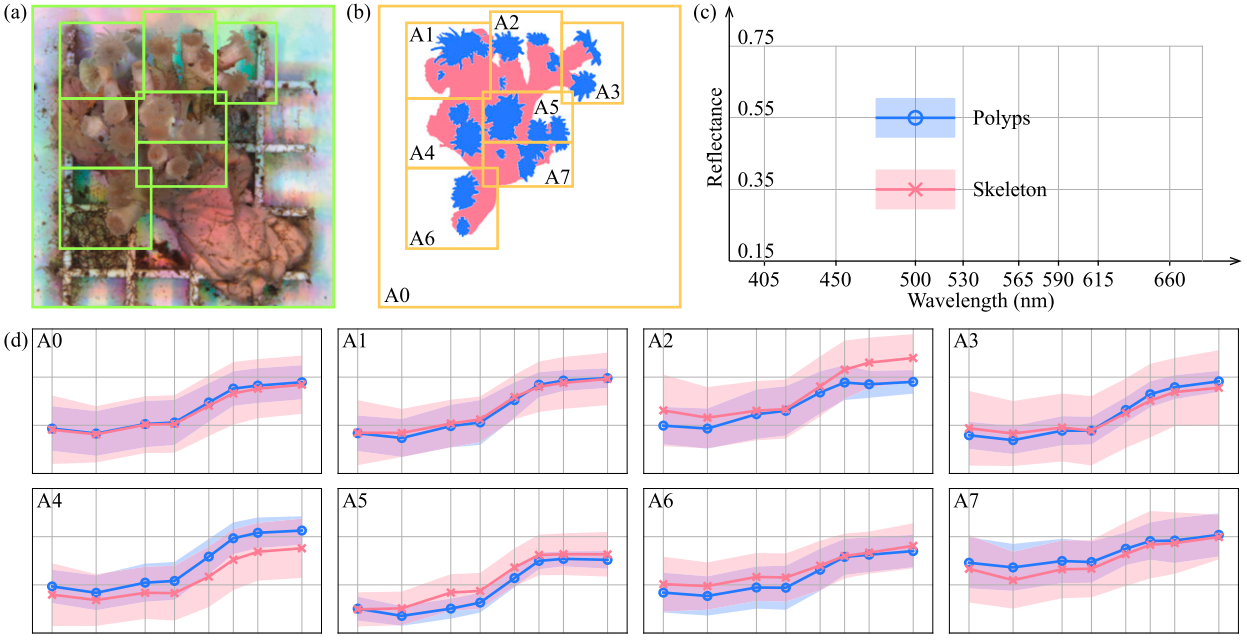

FIG. 11. Averaged spectra of the polyp and skeleton pixels in the MS image shown in Fig. 4. (a) The green frames divide the fused pseudocolor image into seven areas. (b) The annotated polyp and skeleton masks of (a). (d) The averaged spectra of the polyp and skeleton pixels as curves with their standard deviation as shades. (c) Definitions of the axes and legends of all the plots in (d). The varied spectra of polyps and skeletons might result from the different transparency and roughness of the polyps and attached substances on the skeletons.

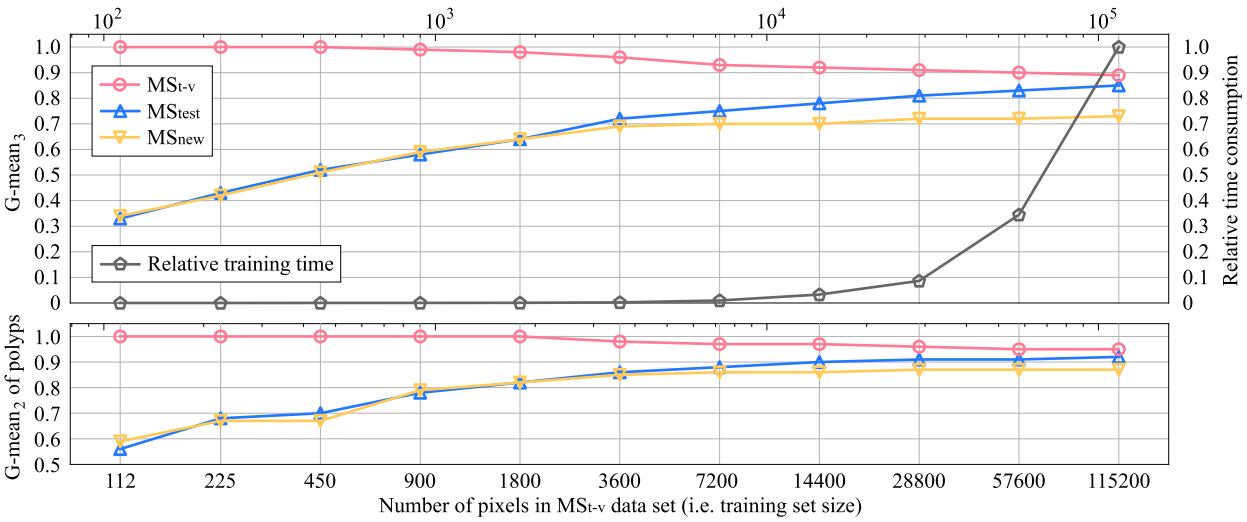

FIG. 12. Performance of MS classifiers with different training set sizes and the corresponding relative time consumptions for training. The time consumptions were normalized by dividing the maximum.

pixels for the three classes. SVM training and classification were performed similar to the procedures described in section 4, and yielded G-mean$_3$ of 0.69, and G-mean$_2$ of 0.88, 0.65, and 0.83 for the polyp–nonpolyp, the skeleton–nonskeleton, and the background–nonbackground binary tests, respectively. Comparing the annotated and estimated polyp activities provided a Pearson correlation coefficient of 0.882 and a root-mean-square deviation of 0.144 among the 36 activity verification images in MS_{act}. By using Fisher's transformation (Fisher 1950), the 95% confidence interval of the Pearson correlation coefficient was calculated as between 0.779 and 0.939. While the annotation effort was much lower than for the full segmentation, the results also attained slightly lower performance values.

6. Conclusions

In this paper, we took advantage of a former proposed tunable LED-based underwater multispectral imaging system for classification and activity estimation of white *Lophelia pertusa* polyps. Results shown that the polyps of *Lophelia pertusa* can be more easily distinguished from its skeletons by analysis of the finer-resolved eight-dimensional spectral reflectance signatures compared to the three-channel RGB data. During a 72-h monitoring with a half-hour temporal resolution in the laboratory, the activity of polyps was estimated based on the results of the multispectral pixel-level classification using SVM classifiers. The estimated polyp activity was consistent with that of the manual annotation, where the correlation coefficient was 0.957 for the verification dataset throughout the 72-h monitoring with an interval of 2 h.

In future studies we will investigate the relationship between spectral absorbance of pigments and imaged spectral reflectance of tissues. Also, we will deploy the low-cost and reliable TuLUMIS system for in situ activity monitoring of *Lophelia pertusa*.

Acknowledgments. This work is supported by China Scholarship Council (201606320111) and German Research Foundation (DFG) Cluster of Excellence FUTURE OCEAN (CP1626). It is Publication 32 of the DeepSea Monitoring group of GEOMAR. The authors express their sincere gratitude to the staff of the GEOMAR Technology and Logistics Centre for their generous technical support, especially to Thorsten Schott, Tim Weiß, and Matthias Wieck. We would also like to thank Yilu Guo (Zhejiang University) and all the colleagues at the DeepSea Monitoring group of GEOMAR, especially to Jochen Mohrmann and Yifan Song, for joining discussions and providing comments. Additionally, Hongbo Liu would like to thank Yufei Jin for her patience, trust, and support.

REFERENCES

Akosa, J., 2017: Predictive accuracy: A misleading performance measure for highly imbalanced data. *SAS Global Forum 2017*, Orlando, FL, SAS Institute, 942–2017, https://support.sas.com/resources/papers/proceedings17/0942-2017.pdf.

Albright, R., and Coauthors, 2016: Reversal of ocean acidification enhances net coral reef calcification. *Nature*, **531**, 362–365, https://doi.org/10.1038/nature17155.

Barnes, C. R., M. M. R. Best, F. R. Johnson, L. Pautet, and B. Pirenne, 2013: Challenges, benefits, and opportunities in installing and operating cabled ocean observatories: Perspectives from NEPTUNE Canada. *IEEE J. Oceanic Eng.*, **38**, 144–157, https://doi.org/10.1109/JOE.2012.2212751.

Baussant, T., M. Nilsen, E. Ravagnan, S. Westerlund, and S. Ramanand, 2018: Effects of suspended drill cuttings on the coral *Lophelia pertusa* using pulsed and continuous exposure scenarios. *J. Toxicol. Environ. Health*, **81A**, 361–382, https://doi.org/10.1080/15287394.2018.1444375.

Bongiorno, D. L., M. Bryson, T. C. L. Bridge, D. G. Dansereau, and S. B. Williams, 2018: Coregistered hyperspectral and stereo image seafloor mapping from an autonomous underwater vehicle. *J. Field Robot.*, **35**, 312–329, https://doi.org/10.1002/rob.21713.

Brooke, S., and C. M. Young, 2009: In situ measurement of survival and growth of *Lophelia pertusa* in the northern Gulf of

Mexico. *Mar. Ecol. Prog. Ser.*, **397**, 153–161, https://doi.org/10.3354/meps08344.

Buhl-Mortensen, P., E. Tenningen, and A. B. S. Tysseland, 2015: Effects of water flow and drilling waste exposure on polyp behaviour in *Lophelia pertusa*. *Mar. Biol. Res.*, **11**, 725–737, https://doi.org/10.1080/17451000.2014.993651.

Büscher, J. V., A. U. Form, and U. Riebesell, 2017: Interactive effects of ocean acidification and warming on growth, fitness and survival of the cold-water coral *Lophelia pertusa* under different food availabilities. *Front. Mar. Sci.*, **4**, 101, https://doi.org/10.3389/fmars.2017.00101.

Dumke, I., S. M. Nornes, A. Purser, Y. Marcon, M. Ludvigsen, S. L. Ellefmo, G. Johnsen, and F. Søreide, 2018a: First hyperspectral imaging survey of the deep seafloor: High-resolution mapping of manganese nodules. *Remote Sens. Environ.*, **209**, 19–30, https://doi.org/10.1016/j.rse.2018.02.024.

——, A. Purser, Y. Marcon, S. M. Nornes, G. Johnsen, M. Ludvigsen, and F. Søreide, 2018b: Underwater hyperspectral imaging as an in situ taxonomic tool for deep-sea megafauna. *Sci. Rep.*, **8**, 12860, https://doi.org/10.1038/s41598-018-31261-4.

Elde, A. C., R. Pettersen, P. Bruheim, J. Järnegren, and G. Johnsen, 2012: Pigmentation and spectral absorbance signatures in deep-water corals from the Trondheimsfjord, Norway. *Mar. Drugs*, **10**, 1400–1411, https://doi.org/10.3390/md10061400.

Erftemeijer, P. L. A., B. Riegl, B. W. Hoeksema, and P. A. Todd, 2012: Environmental impacts of dredging and other sediment disturbances on corals: A review. *Mar. Pollut. Bull.*, **64**, 1737–1765, https://doi.org/10.1016/j.marpolbul.2012.05.008.

Fisher, R. A., 1950: *Statistical Methods for Research Workers*. 11th ed. Oliver and Boyd, 354 pp.

Form, A. U., and Coauthors, 2014: RV Poseidon Cruise Report POS455: LORELEI—Lophelia Reef Lander Expedition and Investigation. GEOMAR Rep., 29 pp., https://doi.org/10.3289/CR_POS_455.

——, and Coauthors, 2015: RV Poseidon Cruise Rep. POS473: LORELEI II—Lophelia Reef Lander Expedition and Investigation II. GEOMAR Rep., 25 pp., https://doi.org/10.3289/CR_POS_473.

Fosså, J. H., P. Mortensen, and D. M. Furevik, 2002: The deep-water coral *Lophelia pertusa* in Norwegian waters: Distribution and fishery impacts. *Hydrobiologia*, **471**, 1–12, https://doi.org/10.1023/A:1016504430684.

Freiwald, A., J. H. Fossa, A. Grehan, T. Koslow, and J. M. Roberts, 2004: Cold-water coral reefs: Out of sight—No longer out of mind. UNEP WCMC Rep. 22, 84 pp.

Godø, O. R., S. Johnsen, and T. Torkelsen, 2014: The LoVe Ocean Observatory is in operation. *Mar. Technol. Soc. J.*, **48**, 24–30, https://doi.org/10.4031/MTSJ.48.2.2.

Greinert, J., and T. Schoening, 2019: RV Poseidon Fahrtbericht/Cruise Report POS526—SeASOM: Semi-Autonomous Subsurface Optical Monitoring for methane seepage and cold-water coral studies in the North Sea. GEOMAR Rep. 051, 86 pp., http://doi.org/10.3289/geomar_rep_ns_51_2019.

Hsu, C.-W., C.-C. Chang, and C.-J. Lin, 2003: A practical guide to support vector classification. National Taiwan University Paper, 16 pp., https://www.csie.ntu.edu.tw/~cjlin/papers/guide/guide.pdf.

Johnsen, G., and Coauthors, 2013: Underwater hyperspectral imagery to create biogeochemical maps of seafloor properties. *Subsea Optics and Imaging*, J. Watson and O. Zielinski, Eds., Electronic and Optical Materials, Woodhead Publishing, 508–535.

——, M. Ludvigsen, A. Sørensen, and L. M. S. Aas, 2016: The use of underwater hyperspectral imaging deployed on remotely operated vehicles—Methods and applications. *IFAC-PapersOnLine*, **49**, 476–481, https://doi.org/10.1016/j.ifacol.2016.10.451.

King, A., S. M. Bhandarkar, and B. M. Hopkinson, 2018: A comparison of deep learning methods for semantic segmentation of coral reef survey images. *Proc. IEEE Conf. on Computer Vision and Pattern Recognition Workshops*, Salt Lake City, UT, IEEE, 1394–1402, https://doi.org/10.1109/CVPRW.2018.00188.

Larsson, A. I., and A. Purser, 2011: Sedimentation on the cold-water coral *Lophelia pertusa*: Cleaning efficiency from natural sediments and drill cuttings. *Mar. Pollut. Bull.*, **62**, 1159–1168, https://doi.org/10.1016/j.marpolbul.2011.03.041.

——, D. van Oevelen, A. Purser, and L. Thomsen, 2013: Tolerance to long-term exposure of suspended benthic sediments and drill cuttings in the cold-water coral *Lophelia pertusa*. *Mar. Pollut. Bull.*, **70**, 176–188, https://doi.org/10.1016/j.marpolbul.2013.02.033.

Letnes, P. A., and Coauthors, 2019: Underwater hyperspectral classification of deep sea corals exposed to a toxic compound. *PLOS ONE*, **14**, e0209960, https://doi.org/10.1371/journal.pone.0209960.

Liu, H., J. Sticklus, K. Köser, H.-J. T. Hoving, H. Song, Y. Chen, J. Greinert, and T. Schoening, 2018: TuLUMIS—A tunable led-based underwater multispectral imaging system. *Opt. Express*, **26**, 7811–7828, https://doi.org/10.1364/OE.26.007811.

Manolakis, D., D. Marden, and G. A. Shaw, 2003: Hyperspectral image processing for automatic target detection applications. *Lincoln Lab. J.*, **14**, 79–116, https://archive.ll.mit.edu/publications/journal/pdf/vol14_no1/14_1hyperspectralprocessing.pdf.

Mobley, C., E. Boss, and C. Roesler, 2018: Ocean Optics Web Book. NASA Ocean Biology and Biochemistry Program, http://www.oceanopticsbook.info/.

Mogstad, A. A., and G. Johnsen, 2017: Spectral characteristics of coralline algae: A multi-instrumental approach, with emphasis on underwater hyperspectral imaging. *Appl. Opt.*, **56**, 9957–9975, https://doi.org/10.1364/AO.56.009957.

Mortensen, P. B., 2001: Aquarium observations on the deep-water coral *Lophelia pertusa* (L., 1758) (scleractinia) and selected associated invertebrates. *Ophelia*, **54**, 83–104, https://doi.org/10.1080/00785236.2001.10409457.

Nilssen, I., T. Möller, and T. W. Nattkemper, 2017: Active learning for the classification of species in underwater images from a fixed observatory. *2017 IEEE Int. Conf. on Computer Vision Workshops*, Venice, Italy, IEEE, 2891–2897, https://doi.org/10.1109/ICCVW.2017.341.

Ødegård, O., A. A. Mogstad, G. Johnsen, A. J. Sørensen, and M. Ludvigsen, 2018: Underwater hyperspectral imaging: A new tool for marine archaeology. *Appl. Opt.*, **57**, 3214–3223, https://doi.org/10.1364/AO.57.003214.

Orejas, C., and Coauthors, 2016: The effect of flow speed and food size on the capture efficiency and feeding behaviour of the cold-water coral *Lophelia pertusa*. *J. Exp. Mar. Biol. Ecol.*, **481**, 34–40, https://doi.org/10.1016/j.jembe.2016.04.002.

Osterloff, J., I. Nilssen, J. Järnegren, P. Buhl-Mortensen, and T. W. Nattkemper, 2016a: Polyp activity estimation and monitoring for cold water corals with a deep learning approach. *2016 ICPR Second Workshop on Computer Vision for Analysis of Underwater Imagery*, Cancun, Mexico, IEEE, https://doi.org/10.1109/CVAUI.2016.013.

——, ——, and T. W. Nattkemper, 2016b: Computational coral feature monitoring for the fixed underwater observatory LoVe. *OCEANS 2016*, Monterey, CA, IEEE, https://doi.org/10.1109/OCEANS.2016.7761417.

——, ——, and ——, 2016c: A computer vision approach for monitoring the spatial and temporal shrimp distribution at the LoVe Observatory. *Methods Oceanogr.*, **15–16**, 114–128, https://doi.org/10.1016/j.mio.2016.03.002.

——, ——, J. Järnegren, T. Van Engeland, P. Buhl-Mortensen, and T. W. Nattkemper, 2019: Computer vision enables short- and long-term analysis of *Lophelia pertusa* polyp behaviour and colour from an underwater observatory. *Sci. Rep.*, **9**, 6578, https://doi.org/10.1038/s41598-019-41275-1.

Pedregosa, F., and Coauthors, 2011: Scikit-learn: Machine learning in Python. *J. Mach. Learn. Res.*, **12**, 2825–2830, https://www.jmlr.org/papers/volume12/pedregosa11a/pedregosa11a.pdf.

Pettersen, R., G. Johnsen, P. Bruheim, and T. Andreassen, 2014: Development of hyperspectral imaging as a bio-optical taxonomic tool for pigmented marine organisms. *Org. Diversity Evol.*, **14**, 237–246, https://doi.org/10.1007/s13127-013-0163-1.

Purser, A., 2015: A time series study of *Lophelia pertusa* and reef megafauna responses to drill cuttings exposure on the Norwegian margin. *PLOS ONE*, **10**, e0134076, https://doi.org/10.1371/journal.pone.0134076.

——, M. Bergmann, T. Lundälv, J. Ontrup, and T. W. Nattkemper, 2009: Use of machine-learning algorithms for the automated detection of cold-water coral habitats: A pilot study. *Mar. Ecol. Prog. Ser.*, **397**, 241–251, https://doi.org/10.3354/meps08154.

——, J. Ontrup, T. Schoening, L. Thomsen, R. Tong, V. Unnithan, and T. W. Nattkemper, 2013: Microhabitat and shrimp abundance within a Norwegian cold-water coral ecosystem. *Biogeosciences*, **10**, 5779–5791, https://doi.org/10.5194/bg-10-5779-2013.

Rimavicius, T., and A. Gelzinis, 2017: A comparison of the deep learning methods for solving seafloor image classification task. *Information and Software Technologies*, R. Damaševičius and V. Mikašytė, Eds., Communications in Computer and Information Science, Vol. 756, Springer, 442–453.

Roberts, J. M., and R. M. Anderson, 2002: A new laboratory method for monitoring deep-water coral polyp behaviour. *Hydrobiologia*, **471**, 143–148, https://doi.org/10.1023/A:1016513607002.

——, A. J. Wheeler, and A. Freiwald, 2006: Reefs of the deep: The biology and geology of cold-water coral ecosystems. *Science*, **312**, 543–547, https://doi.org/10.1126/science.1119861.

——, ——, ——, and S. Cairns, 2009: *Cold-Water Corals: The Biology and Geology of Deep-Sea Coral Habitats*. Cambridge University Press, 351 pp.

Schoening, T., J. Osterloff, and T. W. Nattkemper, 2016: RecoMIA—Recommendations for marine image annotation: Lessons learned and future directions. *Front. Mar. Sci.*, **3**, 59, https://doi.org/10.3389/fmars.2016.00059.

Schölkopf, B., K.-K. Sung, C. J. Burges, F. Girosi, P. Niyogi, T. Poggio, and V. Vapnik, 1997: Comparing support vector machines with Gaussian kernels to radial basis function classifiers. *IEEE Trans. Sig. Proc.*, **45**, 2758–2765, https://doi.org/10.1109/78.650102.

Sture, O., M. Ludvigsen, and L. M. S. Aas, 2017: Autonomous underwater vehicles as a platform for underwater hyperspectral imaging. *OCEANS 2017*, Aberdeen, United Kingdom, IEEE, https://doi.org/10.1109/OCEANSE.2017.8084995.

Tegdan, J., S. Ekehaug, I. M. Hansen, L. M. S. Aas, K. J. Steen, R. Pettersen, F. Beuchel, and L. Camus, 2015: Underwater hyperspectral imaging for environmental mapping and monitoring of seabed habitats. *OCEANS 2015*, Genoa, Italy, IEEE, https://doi.org/10.1109/OCEANS-Genova.2015.7271703.

van Oevelen, D., G. Duineveld, M. Lavaleye, F. Mienis, K. Soetaert, and C. H. R. Heip, 2009: The cold-water coral community as hotspot of carbon cycling on continental margins: A food-web analysis from Rockall bank (northeast Atlantic). *Limnol. Oceanogr.*, **54**, 1829–1844, https://doi.org/10.4319/lo.2009.54.6.1829.

Zawada, D. G., and C. H. Mazel, 2014: Fluorescence-based classification of Caribbean coral reef organisms and substrates. *PLOS ONE*, **9**, e84570, https://doi.org/10.1371/journal.pone.0084570.

Zetsche, E.-M., T. Baussant, F. J. R. Meysman, and D. van Oevelen, 2016: Direct visualization of mucus production by the cold-water coral *Lophelia pertusa* with digital holographic microscopy. *PLOS ONE*, **9**, e0146766, https://doi.org/10.1371/journal.pone.0146766.